Journal of Maps

ISSN: (Print) (Online) Journal homepage: www.tandfonline.com/journals/tjom20

Geology of the Michelangelo quadrangle (H12), Mercury

Salvatore Buoninfante, Valentina Galluzzi, Luigi Ferranti, David A. Rothery, Harald Hiesinger, Laura Guzzetta, Felix Prüße, Benjamin Man, Annie R. Lennox, Alistair Blance, Maurizio Milano & Pasquale Palumbo

To cite this article: Salvatore Buoninfante, Valentina Galluzzi, Luigi Ferranti, David A. Rothery, Harald Hiesinger, Laura Guzzetta, Felix Prüße, Benjamin Man, Annie R. Lennox, Alistair Blance, Maurizio Milano & Pasquale Palumbo (2025) Geology of the Michelangelo quadrangle (H12), Mercury, Journal of Maps, 21:1, 2451791, DOI: 10.1080/17445647.2025.2451791

To link to this article: https://doi.org/10.1080/17445647.2025.2451791

JOURNAL OF MAPS
2025, VOL. 21, NO. 1, 2451791
https://doi.org/10.1080/17445647.2025.2451791

SCIENCE

OPEN ACCESS Check for updates

Geology of the Michelangelo quadrangle (H12), Mercury

Salvatore Buoninfante [a,b], Valentina Galluzzi [b], Luigi Ferranti [a,b], David A. Rothery [c], Harald Hiesinger[d], Laura Guzzetta [e], Felix Prüße[d], Benjamin Man [c], Annie R. Lennox [c], Alistair Blance [c], Maurizio Milano [a] and Pasquale Palumbo [b]

[a]Dipartimento di Scienze della Terra, dell'Ambiente e delle Risorse (DiSTAR), Università degli Studi di Napoli Federico II, Naples, Italy; [b]Istituto di Astrofisica e Planetologia Spaziali (IAPS), INAF, Rome, Italy; [c]School of Physical Sciences, The Open University, Milton Keynes, UK; [d]Institut für Planetologie, Universität Münster, Münster, Germany; [e]Osservatorio Astrofisico di Catania, INAF, Catania, Italy

ABSTRACT

The Michelangelo quadrangle of Mercury (H12) encompasses the area between latitudes 22.5° S–65°S and longitudes 180°E–270°E. The quadrangle covers almost 6.5% of the planet's surface with a total area of almost 5 million km^2. Geologic contacts and linear features were drawn at a mapping scale between 1:300,000 and 1:600,000, based on photointerpretation of MErcury Surface, Space ENvironment, GEochemistry, and Ranging (MESSENGER) Mercury Dual Imaging System (MDIS) imagery. We distinguish three geomorphological plains units (smooth, intermediate, and intercrater plains) and, based on their degradation state, three morpho-stratigraphic classes of craters with diameter ≥ 20 km. The surface of this quadrangle is dominated by intermediate plains and by degraded crater materials of class c2. The geological map at 1:3,000,000 scale improves the existing 1:5,000,000 map based on Mariner-10 data. This work is a contribution to the Mercury geological map series planned to foster observational strategies of the ESA-JAXA BepiColombo mission.

ARTICLE HISTORY
Received 25 July 2024
Revised 31 December 2024
Accepted 3 January 2025

KEYWORDS
Mercury; Geological map series; Michelangelo quadrangle; H12

1. Introduction

Mercury's geology and internal structure have been studied with increasing interest in last decades, leading to a better understanding of the planet's formation and evolution. Mariner 10 (M10) was the first mission that allowed mapping of Mercury's surface. The M10 television experiment (Murray, 1975) observed ~40–45% of the planet's surface during three flybys between 1974 and 1975. Mercury was divided in 15 quadrangles mainly named after prominent topographic features, where M10 coverage data were available, and telescopic albedo features, where image coverage was not available (see Davies et al., 1978; Figure 1). Previous authors provided both complete and partial geological maps at 1:5 million scale (DeHon et al., 1981; Grolier & Boyce, 1984; Guest & Greeley, 1983; King & Scott, 1990; McGill & King, 1983; Schaber & McCauley, 1980; Spudis & Guest, 1988; Spudis & Prosser, 1984; Strom et al., 1990; Trask & Dzurisin, 1984; Trask & Guest, 1975).

The MErcury Surface, Space ENvironment, GEochemistry, and Ranging (MESSENGER) mission was the second mission designed for the exploration of Mercury. The spacecraft performed three flybys of the planet (January 2008, October 2008, and September 2009), and then entered orbit around Mercury on 18 March 2011 (Solomon et al., 2001; Solomon & Anderson, 2018). MESSENGER obtained global image coverage, making possible the first global geological map at a scale of 1:15 million (Kinczyk et al., 2019).

The Michelangelo quadrangle (H12; 180°E–270°E; 22.5°S–65°S) was named after the eponymous crater (44.9°S; 250.3°E), which itself was named by the IAU in 1979. Spudis and Prosser (1984) produced the first geological map of H12 at 1:5 million scale, also including part of the adjacent Neruda quadrangle (H13) as insufficient data were available to provide a separate geological map for H13.

MESSENGER data allowed mapping of H12 at a larger scale thanks to higher resolution end-of-mission datasets (Denevi et al., 2018). So far, several quadrangle maps at 1:3 million scale have been published (Galluzzi et al., 2016; Giacomini et al., 2022, 2024; Guzzetta et al., 2017; Malliband et al., 2023; Man et al., 2023; Mancinelli et al., 2016; Pegg et al., 2021a; Wright et al., 2019) with a coordinated multi-mapper effort to chart the entire planet (Galluzzi, 2019). Galluzzi et al. (2016) and Mancinelli et al. (2016) produced the first geological maps at 1:3 million scale, for Victoria (H02) and Raditladi (H04) quadrangles, respectively. Then, geological maps of Shakespeare (H03; Guzzetta et al., 2017) and Hokusai (H05; Wright

CONTACT Salvatore Buoninfante salvatore.buoninfante@unina.it Dipartimento di Scienze della Terra, dell'Ambiente e delle Risorse (DiSTAR), Università degli Studi di Napoli Federico II, Via Vicinale Cupa Cintia 21, 80126, Naples, Italy; Istituto di Astrofisica e Planetologia Spaziali (IAPS), INAF, Via del Fosso del Cavaliere 100, 00133, Rome, Italy

Supplemental map for this article can be accessed at https://doi.org/10.1080/17445647.2025.2451791.

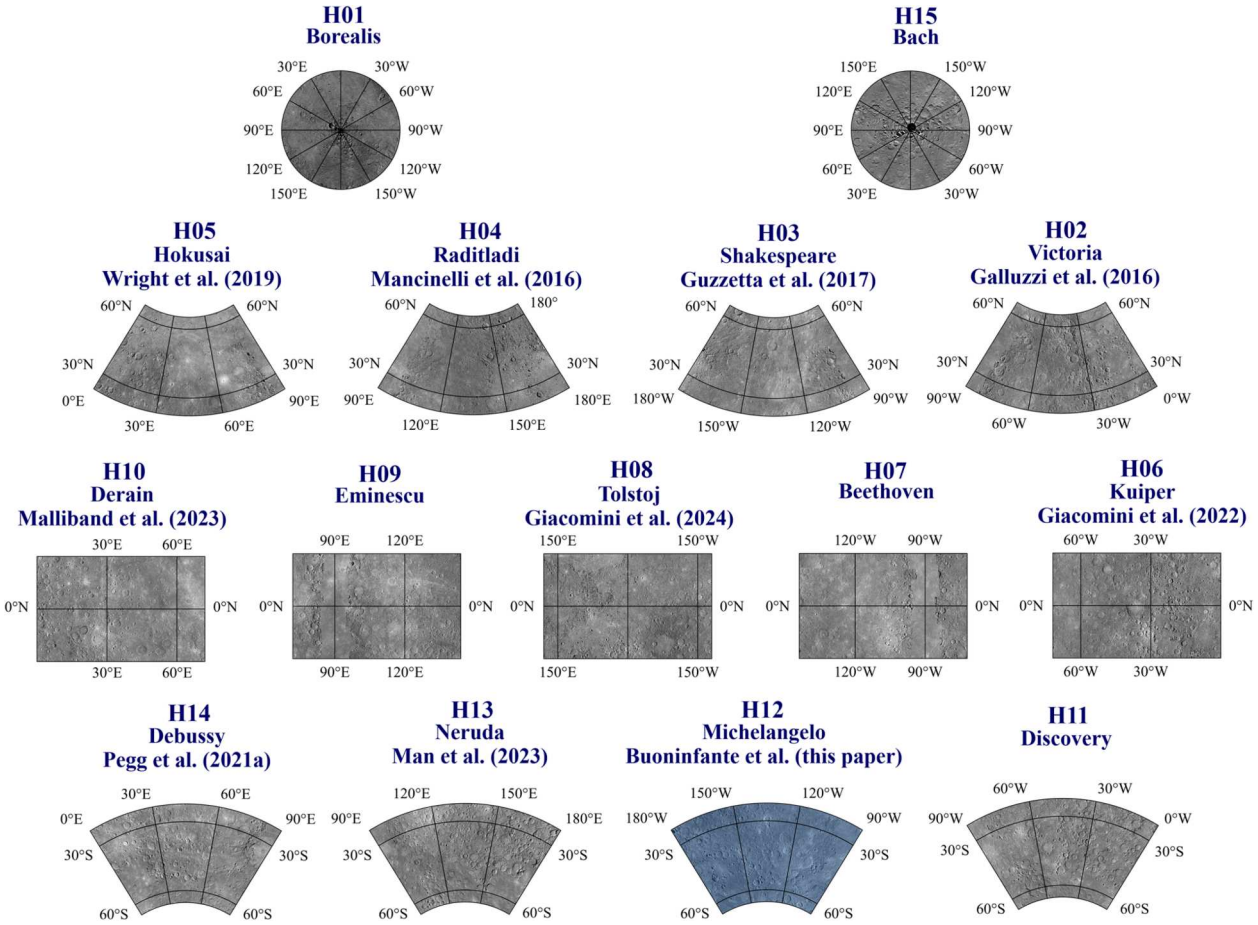

Figure 1. Mercury quadrangles on the MESSENGER MDIS BDR mosaics. The location of the H12 quadrangle (180°E–270°E; 22.5°S–65°S) is highlighted in blue.

et al., 2019) partly completed the 1:3 million scale geological mapping in the northern hemisphere. Pegg et al. (2021a) produced the first 1:3 million scale geological map in the southern hemisphere of Mercury, working on the Debussy (H14) quadrangle. More recently, Giacomini et al. (2022) provided the geological map of the Kuiper (H06) quadrangle, Malliband et al. (2023) produced the geological map of the Derain (H10) quadrangle, while Man et al. (2023) provided the first geological map of Neruda (H13) quadrangle. The last map published by Giacomini et al. (2024) provides the 1:3 million scale geological map of Tolstoj (H08) quadrangle. All maps produced conform to the 1:3 million scale mapping criteria defined in Galluzzi et al. (2016), consisting of a 3-class crater system, although many quadrangle maps have also been produced and published with a 5-class system (e.g. Malliband et al., 2023; Man et al., 2023; Pegg et al., 2021a; Wright et al., 2019). In this work, we present and describe the first geological map of H12 at 1:3 million scale.

2. Data

We used basemaps (Figure 2) produced by the MESSENGER team and derived from the Mercury Dual Imaging System (MDIS) wide-angle camera (WAC) and narrow-angle camera (NAC) data (Denevi et al., 2018; Hawkins et al., 2007). These cameras imaged the planet with a mean resolution of ~200 m/pixel, reaching a maximum of ~8 m/pixel with MDIS/NAC for a total of more than 270,000 images.

The reference basemap used in this work is the MESSENGER MDIS BDR, which is a monochrome mosaic of NAC and WAC 750-nm images, with a resolution of 166 m/pixel (Denevi et al., 2018). The BDR dataset includes mainly moderate solar incidence angle (~74°) images, useful for morphological interpretation.

The LOI basemap consists in a mosaic composed of low incidence angle NAC and WAC 750-nm images with a resolution of 166 m/pixel (Denevi et al., 2018). This product tends to highlight albedo variations and minimize obscuration by shadows.

The HIE and HIW mosaics are derived from NAC and WAC 750-nm images illuminated at high angle of solar incidence (~78°) from the East and West, respectively, with a resolution of 166 m/pixel (Denevi et al., 2018). These basemaps were used to identify morphological features in BDR shadowed regions.

The topographic model used in this work is the global United States Geological Survey (USGS) stereo-

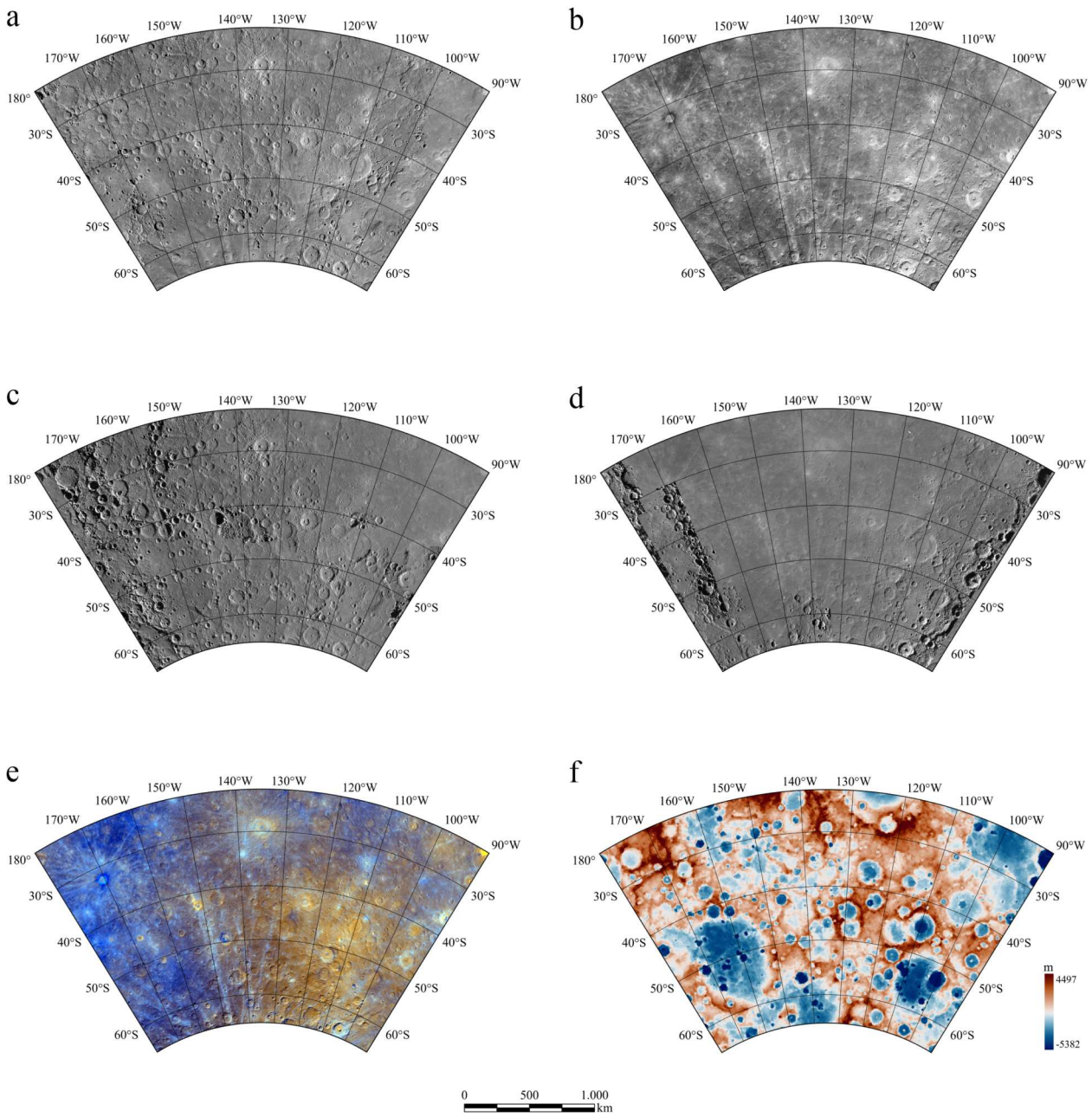

Figure 2. H12 MDIS data used as basemaps for the geological cartography: (a) Basemap reduced Data Record (BDR) mosaic; (b) Low Incidence angle (LOI) mosaic; (c) High Incidence angle from East (HIE) mosaic; (d) High Incidence angle from West (HIW) mosaic; (e) Enhanced Color Basemap mosaic; (f) Digital Elevation Model (DEM).

DEM (665 m/pixel) derived from stereo matching of NAC and WAC 750-nm data with elevations calibrated with the MESSENGER's Mercury Laser Altimeter data (Becker et al., 2016). The global DEM was used in support of monochrome images to better identify tectonic structures and crater rims.

The MESSENGER MDIS 3-color map-projected Multispectral reduced Data record (MD3) was created using MDIS-WAC 1000-nm, 750-nm, 430-nm, filters in the red, green, and blue channels, respectively, at a resolution of ~665 m/pixel. The Enhanced color basemap is a derived MESSENGER product that emphasizes color differences by means of principal component analysis. The second principal component is placed in the red, the first principal component in the green, and the ratio of 430/1000 nm filters in the blue channel, respectively (Denevi et al., 2018). These products were mainly used to identify strongly-colored surface features (i.e. pyroclastic deposits, bright deposits, dark materials, and hollows).

3. Methods

3.1. Map projection

Following previous mid-latitude geological maps (Galluzzi et al., 2016; Guzzetta et al., 2017; Man et al., 2023; Mancinelli et al., 2016; Pegg et al., 2021a; Wright et al., 2019) and standard cartographic guidelines (Davies et al., 1978), the projection used in this

work is the Lambert Conformal Conic (Figures 1 and 2). This projection superimposes a cone on the planet sphere, with two standard parallels that represent the secants between the sphere and the cone of projection, conventionally at 1/6 and 5/6 of the latitudinal range (30°S and 58°S in H12). It is characterized by constant linear deformation and zero angular deformation. The scale of features is true along the standard parallels, slightly smaller between them and slightly larger beyond them (Kennedy & Kopp, 2000).

3.2. Scale

Standard cartographic rules suggest using a mapping scale (Sm) as given by Sm = Rr × 2000, where Rr is the raster resolution (Tobler, 1987). Considering the available spatial resolution of the MESSENGER MDIS BDR reference basemap (~166 m/pixel), the Tobler rule allowed us recognizing features up to 1:300,000-scale. The USGS guidelines recommend mapping at a scale two to five times larger than the final output scale (Tanaka et al., 2011). More recently, Hauber et al. (2019) and Skinner et al. (2022) proposed a mapping scale 4× the publication scale. To exploit MESSENGER basemaps at their best resolution, we drew contacts at a variable scale between ~1:300,000 and ~1:600,000 for a final map-output at 1:3 million scale. We avoided drawing features smaller than 5 km, to avoid feature excess at the chosen output-scale.

3.3. Geodatabase structure and mapping process

Following the USGS recommendations and previous mapping works (e.g. Galluzzi et al., 2016; Giacomini et al., 2022, 2024; Guzzetta et al., 2017; Malliband et al., 2023; Man et al., 2023), we used a geographic information system (GIS) to organize vector layers for the digitization. We created four main feature classes in an ArcGIS Pro 3.2.2 geodatabase: (1) geologic contacts (polyline layer), (2) linear features (polyline layer), (3) geological units (polygon layer), and (4) surface features (polygon layer).

In H12, the linear features include faults, wrinkle ridges, crater rims and irregular pits. We interpreted lobate scarps (e.g. Massironi et al., 2015) and high-relief ridges (e.g. Massironi & Byrne, 2015) as underlain by thrust-faults. Regarding crater rims, we mapped all craters with diameter larger than 5 km.

We classified the degradation state and mapped the ejecta of craters exceeding 20 km in diameter. Geological maps produced using Mariner 10 data (see McCauley et al., 1981) divided craters into five degradation states, directly correlating them to each of the 5 time-periods of Mercury (pre-Tolstojan, Tolstojan, Calorian, Mansurian, Kuiperian). This 5-class system was later updated by Kinczyck et al. (2020) for craters larger than 40 km. Here we follow the approach of Galluzzi et al. (2016), who used a 3-class system, from heavily degraded units (c1) to well-preserved units (c3). The latter approach was devised to resolve rare morphological uncertainties and inconsistencies found when mapping craters larger than 20 km. The 3-class system also allows integration of crater materials into the correlation of map units without implying correspondence to the five chronostratigraphic periods of Mercury. Indeed, by sticking to superposition relationships, this classification enhances the readability of the map at the 1:3M output scale and better frames the stratigraphy of the main volcanic events that shaped the surface in the first billion years of Mercury's history. Indeed, the 3-class system is based on morphostratigraphic interpretation and relies on the stratigraphic correlation of geological units, unlike the 5-class system which is constrained to Mercury's five time periods. The three-class system is currently being used globally in the 1:3M geological map series (Galluzzi et al., 2024), although several maps also use a five-class system in parallel.

Plains units were divided into smooth, intermediate, and intercrater based on the morphological appearance and crater density of the terrains (i.e. from very smooth to rough, respectively). Crater materials and plains units are defined by closed and topographically controlled geological contacts that were subdivided into certain and approximate.

Finally, surface features refer to crater chains, hollows, *faculae*, bright deposits, and dark deposits that locally mantle the main units.

4. Geological map description

4.1. Geological contacts

The geological contacts define the boundaries between the geological units, based on morphological, textural, color, and crater density differences. In this work we subdivided contacts into (a) certain, where there was a clear and sharp contrast between terrain textures or morphologies and (b) approximate, where there was an uncertain, unclear or a gradational transition between terrains.

4.2. Linear features

Linear features include crater rims, tectonic structures and irregular pits. Crater rims are subdivided into (a) 'small' (≥ 5 km and < 20 km in diameter), (b) 'large' (≥ 20 km in diameter) and (c) 'subdued or buried' (≥ 20 km in diameter). 'Subdued or buried' crater rims refer to craters heavily degraded or covered by other units, but whose rim is still morphologically visible.

Tectonic structures include thrusts and faults with uncertain sense of slip. These structures are related

to morphological features known as lobate scarps and high-relief ridges. We mapped separately the wrinkle ridges, which are commonly found in smooth plains or intermediate plains and are interpreted as the surface expression of fault-propagation folds (see Byrne et al., 2018; Klimczak et al., 2019). Fault types are subdivided into: (a) certain, if the faults are very clear and recognizable, and (b) uncertain, if they are inferred or difficult to identify.

Finally, we mapped rims of irregular pits, which are commonly interpreted as the vents formed after explosive eruptions (Jozwiak et al., 2018; Pegg et al., 2021b; Rothery et al., 2014; Thomas et al., 2014a).

4.3. Surface features

Surface features include secondary crater chains (or *catenae*), *faculae*, hollow clusters, bright and dark deposits.

Secondary craters are craters formed by ejecta from larger craters, which can be arranged radially from the crater center, as chains or clusters.

Faculae are very bright features, spectrally red and with diffuse margins. They are thought to represent pyroclastic deposits emplaced by explosive volcanism (Gillis-Davis et al., 2009; Kerber et al., 2011; Pegg et al., 2021b; Thomas et al., 2014a).

Hollows are peculiar features characterized by flat-floored irregular and rimless depressions, surrounded by high-reflectance material, thought to be caused by volatile loss (Blewett et al., 2011; Thomas et al., 2014b; Wang et al., 2020), and usually occurring in clusters.

Bright deposits, unlike the *faculae*, mainly correspond to the ejecta rays of freshest craters. Dark deposits identified in H12 may indicate proximal ejecta enriched in low-reflectance material (or LRM; e.g. Bashō crater; Klima et al., 2018) and exposure of excavated LRM-rich material (e.g. Sibelius crater; Canale et al., 2024).

4.4. Geological units

4.4.1. Plains units

We recognized and mapped three different plains in H12: smooth, intermediate and intercrater plains, from younger to older respectively.

Smooth plains are defined as flat or sparsely cratered surfaces with a smooth texture (Spudis & Guest, 1988; Strom et al., 1975; Trask & Guest, 1975) and they may encompass well recognizable ghost craters (see Head et al., 2008; Klimczak et al., 2012). In H12 sp are uncommon and mostly confined to impact basins and craters or formed as patches of ejecta (Figure 3a,b). Clear examples of sp inside H12 can be found inside the Michelangelo crater (44.9°S–250.3°E), Takayoshi crater (37.2°S–196.2°E) and the Beethoven basin (20.9°S–235.8°E). Patches of smooth plains were mainly detected in the proximal ejecta of the Beethoven basin. Based on the Enhanced color basemap observations, sp in the H12 quadrangle seems to be characterized by consistent reflectance characteristics, implying compositional homogeneity. Wrinkle ridges can be frequently identified inside sp. At the planet scale, most smooth plains are interpreted as the result of effusive volcanism that affected Mercury during the Calorian (~3.8–3.5 Ga; Byrne et al., 2016; Denevi et al., 2013; Ostrach et al., 2015). Within ancient craters and basins, these units represent the most recent effusive event, as later impact craters on the floor of these basins embayed or covered by the infilling lavas. Patches of smooth plains identified in the proximal ejecta of craters or basins are interpreted as ponds of impact melt (see also Wright et al., 2019).

The intermediate plains are plains with characteristics intermediate between intercrater and smooth plains. They are represented by smooth undulating to planar surfaces and are more cratered than sp, but less cratered than the intercrater plains (Spudis & Prosser, 1984). This unit is characterized by smooth to hummocky terrain, overprinted by sharp to degraded crater rims. In H12, imp represents the most widespread unit. In many cases imp covers the floor of large ancient basins, and was probably formed by later infilling, then, degraded by younger impacts (Figure 3c,d). The transition between intermediate and intercrater plains is usually subdued and of gradational appearance. The identification of wrinkle ridges was useful as a distinction, because imp may also be characterized by the presence of these structures, even if not so commonly as in smooth plains (e.g. Galluzzi et al., 2016). Imp may include embayed craters, which is a key characteristic of units younger than intercrater plains. The imp shows spectral characteristics very similar to the icp in H12 and tends to correspond with darker areas observed in the Enhanced color basemap mainly in the western sector of the quadrangle. In some mapped quadrangles, imp is interpreted as a thin layer of smooth plains covering intercrater plains thus preserving the underlying roughness (Wright et al., 2019). However, since in our work we also consider the stratigraphic interpretation of the geological units, intermediate plains are mapped where these are thought to be a defined unit of intermediate age and intermediate texture between smooth plains and intercrater plains. Areas texturally consistent with imp, but with superposing crater density lower than average imp crater density, are considered as thin layer of sp and thus mapped as such by sticking to stratigraphic laws. Instead, where crater density cannot be easily assessed because of morphological uncertainties, the unit is mapped as imp.

The intercrater plains are densely cratered surfaces, considered as the most widespread unit on Mercury

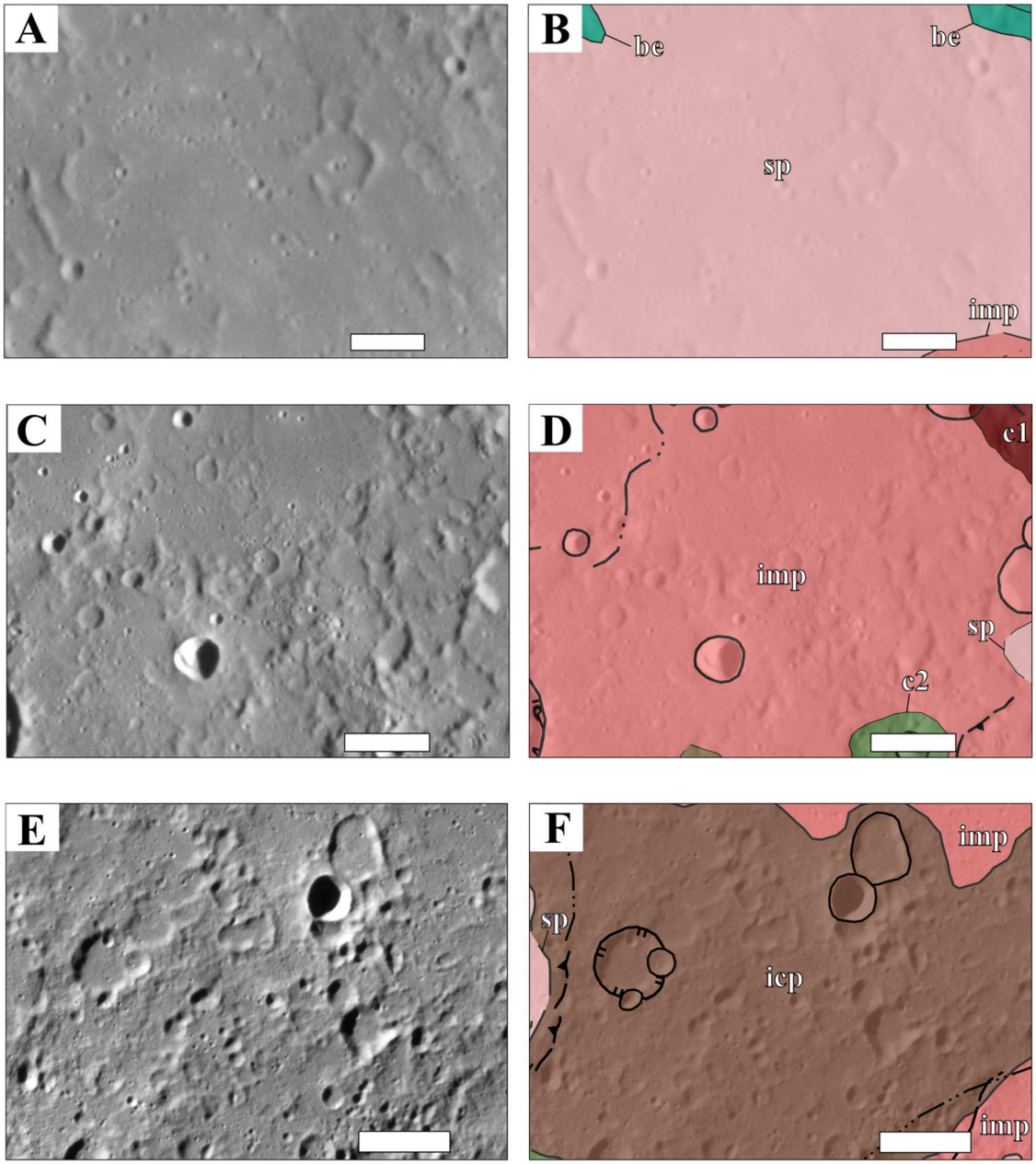

Figure 3. Examples of plains units (BDR mosaic basemap on the left and the geological interpretation on the right): (a, b): smooth plains (sp); (c, d): intermediate plains (imp); (e, f): intercrater plains (icp). Legend in the main map. Reference scale is 10 km for (a) and (b), 20 km for (c) and (d), 25 km for (e) and (f).

(e.g. Kinczyk et al., 2018; Trask & Guest, 1975; Whitten et al., 2014). The texture is rough and hummocky, previously described by Trask and Guest (1975) as 'level to gently rolling ground between and around large craters and basins'. They are globally characterized by isostatic gravity anomaly lows (see Buoninfante et al., 2023). A pre-Tolstojan to Tolstojan age (4.5–3.9 Ga; Whitten et al., 2014) is assigned to this unit, which is considered as the oldest surface on Mercury. In H12 icp represent the second most widespread unit (Figure 3e,f). The intercrater plains can be superposed by all three crater classes (c1–c3), and frequently by degraded secondary impact craters (Whitten et al., 2014). They lack distinct spectral characteristics and specific colors. These plains may have a volcanic origin, although heavily degraded and reworked by later impacts (Marchi et al., 2013; Whitten et al., 2014).

4.4.2. Crater materials units

According to the three degradation-class system we identified three classes of crater materials (Figure 4): from the youngest and well-preserved showing fresher morphology (c3) to the oldest and most degraded (c1).

Fresh craters (c3) are craters with sharp and intact rims. When complex, they can be characterized by a well-preserved central peak or peak ring, and by well-defined terraces and textured ejecta blankets. Contacts between crater floor and the wall or internal structures are also well-defined. Ejecta are usually very

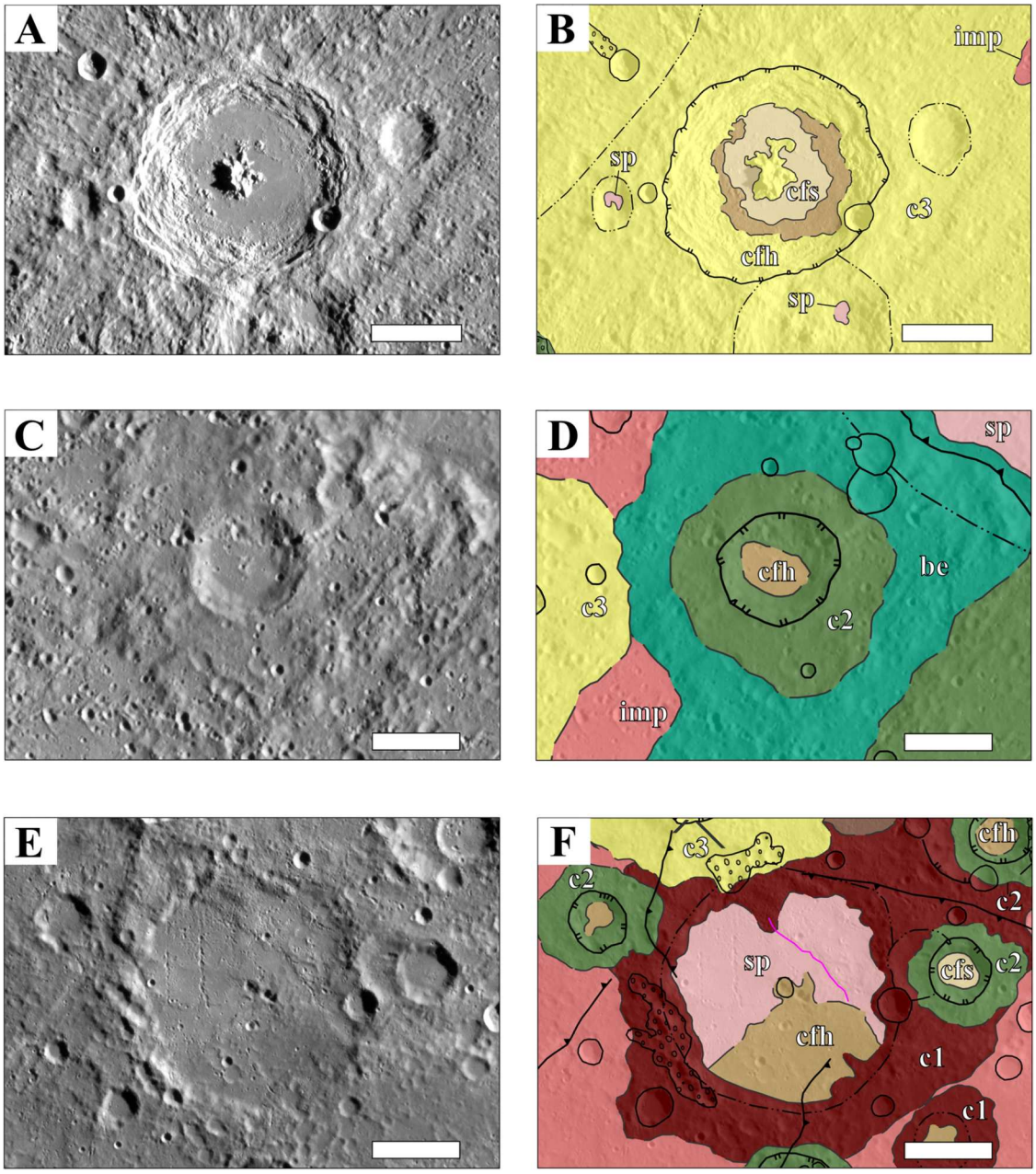

Figure 4. Examples of crater materials based on degradation degree (BDR mosaic basemap on the left and the geological interpretation on the right): fresh crater (Bartók crater; c3), degraded crater (c2), heavily degraded crater (c1) from top to bottom, respectively. Smooth crater floors are indicated as 'cfs'; hummocky crater floors are indicated as 'cfh'. Legend in the main map. Reference scale is 50 km for (a) and (b), 30 km for (c–f).

distinct and bright, and recognizable up to one diameter, sometimes wider, from the crater rim. Evident striations, crater chains, or even rays can be locally detected, and distal ejecta are well-identified by small secondary craters.

Degraded craters (c2) identify craters moderately degraded, with complete or partially subdued rims, usually not sharp. In complex craters, wall terraces can be present, but not well-defined. Central peaks or peak rings appear subdued. Ejecta can still be distinct, but often they are less than one diameter away from the rim. Also, distal ejecta are more difficult to discern.

Highly degraded craters (c1) define degraded craters with eroded or erased rims. These are usually larger in size and therefore likely formed as complex craters. Central peaks or peak rings are usually degraded or absent. The contact between the crater floor and the wall or internal structures is usually approximate. Only proximal ejecta close to the rim can be discerned. These craters are often degraded by several later impacts of all sizes. They may also present ruptures of crater rims and be embayed by sp or imp.

Smooth crater floors (cfs) indicate smooth and planar crater floors, scarcely affected by later impacts. Smooth floors may represent the original and likely young floor of fresher impact craters (c3), volcanic infilling or impact melt following the impact (e.g.

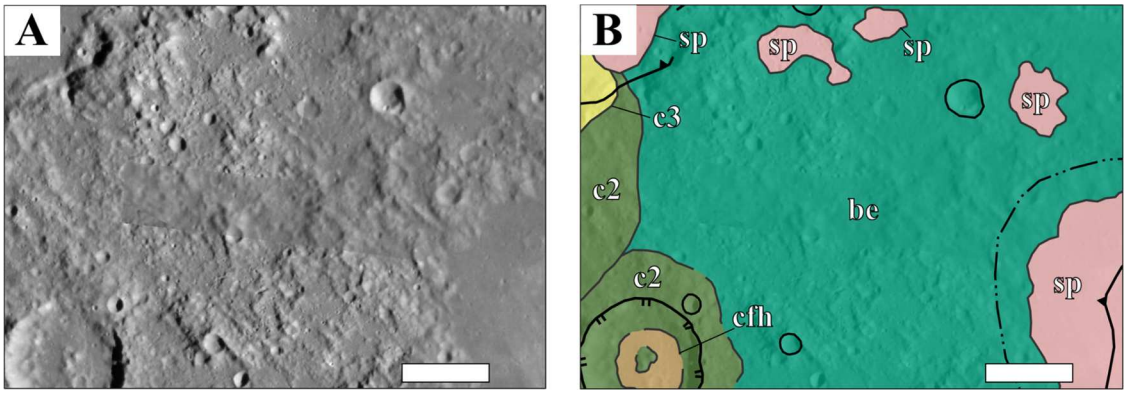

Figure 5. Example of Beethoven basin ejecta (Be). (a) BDR mosaic; (b) Interpreted geological map. Legend in the main map. Reference scale is 25 km.

Canale et al., 2024). Smooth plains unit (sp) covering basin floor represents later infilling and differs from smooth crater floors unit (cfs) interpreted as the original floor material.

Hummocky crater floors (cfh) identify crater floor with rough texture or gently rolling material. In c3 or c2 craters, these materials represent crater wall debris, mass wasting deposits or the original floor. In more degraded craters, this unit represents a degraded floor caused by subsequent small impacts.

The Beethoven basin (20.9°S–235.8°E) extends between H12 and H07 quadrangles, with a diameter of ~640 km, and is thought to have a Tolstojan age (Spudis & Guest, 1988). We mapped Beethoven basin ejecta as a separate geological unit (Figure 5) because they have spectral characteristics slightly different to the adjacent terrains, appearing with darker colors in the Enhanced Color Basemap. This suggests that they are characterized by a different composition. The ejecta extend almost one diameter from the basin rim, but on the western side they appear almost completely covered by more recent units (intermediate plains, degraded or fresh crater materials). On the eastern side, the basin ejecta unit is superimposed by multiple patches of smooth plains, which in some cases fill subdued impact craters.

5. Discussion

5.1. Correlation of geological units

The Michelangelo quadrangle is a densely cratered quadrangle, mainly dominated by imp and by c2 crater materials. The imp can be usually found inside large ancient basins, interpreted as post-impact infilling by effusive volcanism, and degraded by later small impacts and by their ejecta materials. Clear examples can be seen in Dostoevskij crater (44.7°S–181.9°E), Vincente-Yakovlev basin (52.6°S–197.9°E, Orgel et al., 2020) and the b2 basin (38.9°S–258.6°E, Orgel et al., 2020). The Michelangelo crater and the Beethoven basin are characterized by smooth plains units covering the basin floors. Smooth and intermediate plains in H12 are frequently affected by wrinkle ridges with various orientations. The quadrangle is also characterized by the significant presence of younger craters with well-preserved materials (c3). Intercrater plains represent the second most extensive terrain within H12, while smooth plains are mainly confined to some crater interiors, and to some patches interpreted as fluidized ejecta deposits (see also Denevi et al., 2013). Based on the Enhanced color basemap, we can mainly identify a dark blue terrain in the western side (180–200°E), and bright reddish and yellow terrains covering almost all the rest of the quadrangle. The bright reddish terrains show the same spectral characteristics as the high-reflectance plains (HRP; Robinson et al., 2008). Comparing the mapped geological units and the Enhanced color basemap, the c3 craters and smooth plains tend to overlap with the yellow bright areas. While the dark blue terrains are spatially comparable with the intermediate plains covering ancient basin floors and Beethoven ejecta. This also suggests a possible compositional difference between the 'dark' infilling (imp) of ancient basins, such as Vincente-Yakovlev (Orgel et al., 2020), and the 'bright' infilling (sp) of younger basins and craters such as Beethoven and Michelangelo.

The schematic stratigraphy shown in Figure 6 represents the correlation between H12 geological units, based on the superposition relationships observed and on previously estimated absolute model ages (Byrne et al., 2016; Giacomini et al., 2022; Marchi et al., 2013; Neukum et al., 2001; Ostrach et al., 2015; Whitten et al., 2014). A complete schematic correlation of map units is shown in the main map attachment.

5.2. The Beethoven basin

The Beethoven basin has a subdued rim (King & Scott, 1990; Spudis & Guest, 1988; Spudis & Prosser, 1984; Strom et al., 1975). The basin floor is constituted by smooth plains materials formed by later

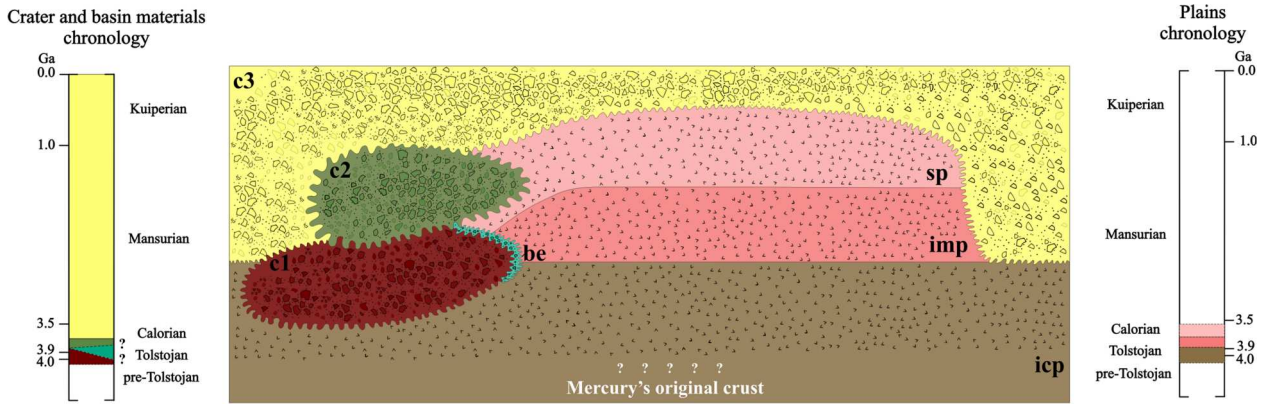

Figure 6. Chronostratigraphic scheme of Mercury (see also Galluzzi et al., 2016) related to plains units (icp, imp, sp; right) and crater and basin materials (be, c1, c2, c3; left). Mercury's geochronology from Spudis and Guest (1988). Ga: billions of years. The stratigraphic column (not to scale) shows the correlation of H12 geological units based on superposition criteria and absolute model ages (Byrne et al., 2016; Giacomini et al., 2022; Marchi et al., 2013; Neukum et al., 2001; Ostrach et al., 2015; Whitten et al., 2014). The undulating lines represent erosional contacts. Brecciated texture is used for crater materials symbology, while arrow heads indicate plains units.

infilling (King & Scott, 1990; Spudis & Guest, 1988; Spudis & Prosser, 1984), with estimated age of 3.7–3.9 Ga (Byrne et al., 2016; Massironi et al., 2009). The sp unit may have buried internal rings (Spudis & Guest, 1988). Beethoven is superposed by five main c3 to c2 craters, especially Bello crater (c3, 18.9°S–239.8°E) and Sayat-Nova crater (c2, 28.0°S–237.3°E), and their respective ejecta materials. It is noteworthy that the main tectonic structures within the basin display a concentric pattern, consistently with what has already been shown for some ancient large impact basins (e.g. Fassett et al., 2012; Fegan et al., 2017; Orgel et al., 2020; Rothery, 2015). Fegan et al. (2017) suggested fault nucleation along the interface between the basin floor and the younger smooth plains units covering the floor. In the case of Beethoven, the presence of an external NW–SE fault segment that links to the internal concentric structure, suggests that this NW–SE thrust system could potentially be deeper and continue along a preferential weakness plane inside the basin. Duyfken Rupes (20.9°S–228.1°E) is the main concentric thrust segment and lies close to and inside the basin rim. This structure is part of a major thrust system trending NW–SE. Important thrust segments are also identified in the southern and eastern edges of the Beethoven basin, partly or completely cutting the superposed craters, thus showing that the tectonic activity is younger than the basin and craters. The mapped concentric faults bordering the inner depression of the basin can be interpreted as normal or oblique faults developed after the impact due to gravitational subsidence (e.g. Melosh, 1996). Wrinkle ridges inside the basin affect the sp units and developed mostly concentrically. Our mapping shows that the Beethoven basin materials must be older than the intermediate plains and c2 craters. Stratigraphic relationships confirm a probable Tolstojan-Early Calorian age for Beethoven, between 4.0 and 3.8 Ga.

6. Summary

We produced a geological map of the Michelangelo quadrangle (H12) at a scale of 1:3 million, from photo-interpretation of MESSENGER MDIS imagery. This product represents an improvement on the previous geological map of H12 at 1:5 million scale compiled after the Mariner 10 mission (Spudis & Prosser, 1984). We used the same cartographic criteria adopted in the previous geological map series at 1:3 million scale using MESSENGER data (Galluzzi et al., 2016; Giacomini et al., 2022, 2024; Guzzetta et al., 2017; Malliband et al., 2023; Man et al., 2023; Mancinelli et al., 2016; Pegg et al., 2021a; Wright et al., 2019). Michelangelo is mostly dominated by degraded crater materials (c2) and intermediate plains (imp), which are frequently observed inside large ancient basins and interpreted as later degraded infilling. We have spectrally identified two main types of terrains: dark and blue terrains, and bright reddish and yellow terrains. This also suggests putative compositional difference between the imp of ancient basins and the sp identified in the younger basins of H12. Beethoven basin is a Tolstojan-Early Calorian basin (~4.0–3.8 Ga), whose floor was later filled by smooth plains unit. The main tectonic structures inside the basin have a concentric pattern, and their activity is younger than the basin and overlapping craters. The NW-SE trending structures are also part of the major thrust system identified in H12. The H12 geological map represents a contribution to the geological map series at 1:3 million scale (Galluzzi et al., 2024), useful for supporting observational strategies and scientific goals of the ESA-JAXA's BepiColombo mission (Benkhoff et al., 2021; Rothery et al., 2020).

Software

We used ArcGIS Pro 3.2.2. Geographic Information System software to produce maps. The main map was completed in Adobe Illustrator.

Acknowledgements

The authors acknowledge the use of MESSENGER MDIS data (Monochrome basemaps, Color mosaic, Enhanced Color mosaics and DEM), downloaded from Planetary Data System (PDS) archive. The authors sincerely thank Christian Klimczak, Makram Murad-al-shaikh and the Associate Editor Monica Pondrelli for their insightful reviews of the manuscript and map.

Disclosure statement

No potential conflict of interest was reported by the author(s).

Funding

This work is part of S. B. PhD project at the Department of Earth, Environment and Resources at the University of Naples, Italy and was funded by Italian Space Agency (ASI) under ASI-INAF agreement 2024-18-HH.0. The UK Research and Innovation (UKRI) Science and Technology Facilities Council (STFC) and the Open University's Strategic Research Area in Space funded PhD research by Man, Lennox and Blance.

Data availability statement

All basemap data are publicly available from NASA's Planetary Data System (https://pds-imaging.jpl.nasa.gov/portal/). Shapefiles and digital copy of the map are freely available upon request.

ORCID

Salvatore Buoninfante http://orcid.org/0000-0003-2596-9267
Valentina Galluzzi http://orcid.org/0000-0002-3237-3456
Luigi Ferranti http://orcid.org/0000-0002-0531-6763
David A. Rothery http://orcid.org/0000-0002-9077-3167
Laura Guzzetta http://orcid.org/0000-0003-3619-1032
Benjamin Man http://orcid.org/0000-0001-9056-6072
Annie R. Lennox http://orcid.org/0009-0003-9305-6512
Alistair Blance http://orcid.org/0000-0002-9136-8438
Maurizio Milano http://orcid.org/0000-0002-8907-6428
Pasquale Palumbo http://orcid.org/0000-0003-2323-9228

References

Becker, K. J., Robinson, M. S., Becker, T. L., Weller, L. A., Edmundson, K. L., Neumann, G. A., Perry, M. E., & Solomon, S. C. (2016). First global digital elevation model of mercury. In *47th lunar and planetary science conference* (p. 2959). Abstract No. 1903.

Benkhoff, J., Murakami, G., Baumjohann, W., Besse, S., Bunce, E., Casale, M., Cremosese, G., Glassmeier, K.-H., Hayakawa, H., Heyner, D., Hiesinger, H., Huovelin, J., Hussmann, H., Iafolla, V., Iess, L., Kasaba, Y., Kobayashi, M., Milillo, A., Mitrofanov, I. G., … Zender, J. (2021). BepiColombo - Mission Overview and Science Goals. *Space Science Reviews*, *217*(8), 7413. http://dx.doi.org/10.1007/s11214-021-00861-4

Blewett, D. T., Chabot, N. L., Denevi, B. W., Ernst, C. M., Head, J. W., Izenberg, N. R., Murchie, S. L., Solomon, S. C., Nittler, L. R., McCoy, T. J., Xiao, Z., Baker, D. M. H., Fassett, C. I., Braden, S. E., Oberst, J., Scholten, F., Preusker, F., & Hurwitz, D. M. (2011). Hollows on Mercury: MESSENGER evidence for geologically recent volatile-related activity. *Science*, *333*(6051), 1856–1859. https://doi.org/10.1126/science.1211681

Buoninfante, S., Milano, M., Negri, B., Plainaki, C., Sindoni, G., & Fedi, M. (2023). Gravity evidence for a heterogeneous crust of Mercury. *Scientific Reports*, *13*(19854), 1–11. https://doi.org/10.1038/s41598-023-46081-4

Byrne, P. K., Klimczak, C., & Celâl Şengör, A. M. (2018). The tectonic character of Mercury. In S. C. Solomon, L. R. Nittler, & B. J. Anderson (Eds.), *Mercury: The view after MESSENGER* (pp. 249–286). Cambridge University Press. https://doi.org/10.1017/9781316650684.011

Byrne, P. K., Ostrach, L. R., Fassett, C. I., Chapman, C. R., Denevi, B. W., Evans, A. J., & Solomon, S. C. (2016). Widespread effusive volcanism on Mercury likely ended by about 3.5 Ga. *Geophysical Research Letters*, *43*(14), 7408–7416. https://doi.org/10.1002/2016GL069412

Canale, M., Wright, J., & Rothery, D. A. (2024). A hybrid geological map of Sibelius Crater on Mercury, and its associated ejecta and impact melt deposits. *Geological Society, London, Special Publications*, *541*(1), 153–180. https://doi.org/10.1144/SP541-2022-296

Davies, M. E., Dwornik, S. E., Gault, D. E., & Strom, R. G. (1978). *Atlas of Mercury*.

DeHon, R. A., Scott, D. H., & Underwood, J. R. (1981). *Geologic Map of the Kuiper Quadrangle of Mercury*.

Denevi, B. W., Chabot, N. L., Murchie, S. L., Becker, K. J., Blewett, D. T., Domingue, D. L., Ernst, C. M., Hash, C. D., Hawkins, S. E., Keller, M. R., ..., & Solomon, S. C. (2018). Calibration, projection, and final image products of MESSENGER's mercury dual imaging system. *Space Science Reviews*, *214*(2), 1–52. https://doi.org/10.1007/s11214-017-0440-y

Denevi, B. W., Ernst, C. M., Meyer, H. M., Robinson, M. S., Murchie, S. L., Whitten, J. L., Head, J. W., Watters, T. R., Solomon, S. C., Ostrach, L. R., Chapman, C. R., Byrne, P. K., Klimczak, C., & Peplowski, P. N. (2013). The distribution and origin of smooth plains on Mercury. *Journal of Geophysical Research: Planets*, *118*(5), 891–907. https://doi.org/10.1002/jgre.20075

Fassett, C. I., Head, J. W., Baker, D. M. H., Zuber, M. T., Smith, D. E., Neumann, G. A., Solomon, S. C., Klimczak, C., Strom, R. G., Chapman, C. R., Prockter, L. M., Phillips, R. J., Oberst, J., & Preusker, F. (2012). Large impact basins on Mercury: Global distribution, characteristics, and modification history from MESSENGER orbital data. *Journal of Geophysical Research: Planets*, *117*(E12), 1–15. https://doi.org/10.1029/2012JE004154

Fegan, E. R., Rothery, D. A., Marchi, S., Massironi, M., Conway, S. J., & Anand, M. (2017). Late movement of basin-edge lobate scarps on Mercury. *Icarus*, *288*, 226–234. https://doi.org/10.1016/j.icarus.2017.01.005

Galluzzi, V. (2019). Multi-mapper projects: Collaborative Mercury mapping. In H. Hargitai (Ed.), *Planetary cartography and GIS, lecture notes in geoinformation and*

cartography (pp. 207–218). Springer, Cham. https://doi.org/10.1007/978-3-319-62849-3_9

Galluzzi, V., Guzzetta, L. G., Ferranti, L., Di Achille, G., Rothery, D. A., & Palumbo, P. (2016). Geology of the Victoria quadrangle (H02), Mercury. *Journal of Maps*, *12*(sup1), 227–238. https://doi.org/10.1080/17445647.2016.1193777

Galluzzi, V., Rothery, D. A., Blance, A., Buoninfante, S., Giacomini, L., Guzzetta, L., Lennox, A. R., Man, B., Sepe, A., Tognon, G., Wright, J., Massironi, M., & Ferranti, L. (2024). *Update on the Quadrangle Geological Map Series of Mercury*. Abstract Booklet, Mercury 2024, Kyoto, Japan.

Giacomini, L., Galluzzi, V., Massironi, M., Ferranti, L., & Palumbo, P. (2022). Geology of the Kuiper quadrangle (H06), Mercury. *Journal of Maps*, *18*(2), 246–257. https://doi.org/10.1080/17445647.2022.2035268

Giacomini, L., Guzzetta, L., Galluzzi, V., Ferranti, L., & Palumbo, P. (2024). Geology of Tolstoj quadrangle (H08), Mercury. *Journal of Maps*, *20*(1), 2421600. https://doi.org/10.1080/17445647.2024.2421600

Gillis-Davis, J. J., Blewett, D. T., Gaskell, R. W., Denevi, B. W., Robinson, M. S., Strom, R. G., Solomon, S. C., & Sprague, A. L. (2009). Pit-floor craters on Mercury: Evidence of near-surface igneous activity. *Earth and Planetary Science Letters*, *285*(3-4), 243–250. https://doi.org/10.1016/j.epsl.2009.05.023

Grolier, M. J., & Boyce, J. M. (1984). *Geologic Map of the Borealis region (H-1) of Mercury*. USGS Miscellaneous Investigations Series Map I–1660 1–1.

Guest, J. E., & Greeley, R. (1983). *Geologic Map of the Shakespeare (H–3) Quadrangle of Mercury*. USGS Miscellaneous Investigations Series, Map I–1408.

Guzzetta, L. G., Galluzzi, V., Ferranti, L., & Palumbo, P. (2017). Geology of the Shakespeare quadrangle (H03), Mercury. *Journal of Maps*, *13*(2), 227–238. https://doi.org/10.1080/17445647.2017.1290556

Hauber, E., Naß, A., Skinner, J. A., & Huff, A.. (2019). Planetary Geologic Mapping. In *Hargitai, H. (eds) Planetary Cartography and GIS. Lecture Notes in Geoinformation and Cartography*. Springer, Cham. https://doi.org/10.1007/978-3-319-62849-3_5

Hawkins, S. E., Boldt, J. D., Darlington, E. H., Espiritu, R., Gold, R. E., Gotwols, B., Grey, M. P., Hash, C. D., Hayes, J. R., Jaskulek, S. E., & Kardian, C. J. (2007). The Mercury dual imaging system on the MESSENGER spacecraft. *Space Science Reviews*, *131*, 247–338. https://doi.org/10.1007/s11214-007-9266-3

Head, J. W., Murchie, S. L., Prockter, L. M., Robinson, M. S., Solomon, S. C., Strom, R. G., Chapman, C. R., Watters, T. R., McClintock, W. E., Blewett, D. T., & Gillis-Davis, J. J. (2008). Volcanism on Mercury: Evidence from the first MESSENGER flyby. *Science*, *321*(5885), 69–72. https://doi.org/10.1126/science.1159256

Jozwiak, L. M., Head, J. W., & Wilson, L. (2018). Explosive volcanism on Mercury: Analysis of vent and deposit morphology and modes of eruption. *Icarus*, *302*, 191–212. https://doi.org/10.1016/j.icarus.2017.11.011

Kennedy, M., & Kopp, S. (2000). Understanding Map projections GIS by ESRI. In *GIS by ESRI* (pp. 1–112). Environmental Systems Research Institute, Inc.

Kerber, L., Head, J. W., Blewett, D. T., Solomon, S. C., Wilson, L., Murchie, S. L., Robinson, M. S., Denevi, B. W., & Domingue, D. L. (2011). The global distribution of pyroclastic deposits on Mercury: The view from MESSENGER flybys 13. *Planetary and Space Science*, *59*(15), 1895–1909. https://doi.org/10.1016/j.pss.2011.03.020

Kinczyk, M. J., Prockter, L. M., Byrne, P. K., Denevi, B. W., Buczkowski, D. L., Ostrach, L. R., & Miller, E. B. (2019). The first global geological map of Mercury. *EPSC-DPS Joint Meeting*, *13*, 1045.

Kinczyk, M. J., Prockter, L. M., Byrne, P. K., Denevi, B. W., Ostrach, L. R., & Skinner, J. A. (2018). *A global geological map of Mercury*. Mercury: Current and future science of the innermost planet, Columbia, Maryland, Abstract #6123.

Kinczyk, M. J., Prockter, L. M., Byrne, P. K., Susorney, H. C. M., & Chapman, C. R. (2020). A morphological evaluation of crater degradation on Mercury: Revisiting crater classification with MESSENGER data. *Icarus*, *341*, 113637. http://dx.doi.org/10.1016/j.icarus.2020.113637

King, J. S., & Scott, D. H. (1990). *Geologic Map of the Beethoven Quadrangle of Mercury*. USGS Miscellaneous Investigations Series, Map I–2048.

Klima, R. L., Denevi, B. W., Ernst, C. M., Murchie, S. L., & Peplowski, P. N. (2018). Global distribution and spectral properties of low-reflectance material on Mercury. *Geophysical Research Letters*, *45*(7), 2945–2953. https://doi.org/10.1002/2018GL077544

Klimczak, C., Byrne, P. K., Şengör, A. M. C., & Solomon, S. C. (2019). Principles of structural geology on rocky planets. *Canadian Journal of Earth Sciences*, *56*(12), 1437–1457. https://doi.org/10.1139/cjes-2019-0065

Klimczak, C., Watters, T. R., Ernst, C. M., Freed, A. M., Byrne, P. K., Solomon, S. C., Blair, D. M., & Head, J. W. (2012). Deformation associated with ghost craters and basins in volcanic smooth plains on Mercury: Strain analysis and implications for plains evolution. *Journal of Geophysical Research: Planets*, *117*(E12). https://doi.org/10.1029/2012JE004100

Malliband, C. C., Rothery, D. A., Balme, M. R., Conway, S. J., Pegg, D. L., & Wright, J. (2023). Geology of the Derain quadrangle (H10), Mercury. *Journal of Maps*, *19*(1), 1–10. https://doi.org/10.1080/17445647.2022.2112774

Man, B., Rothery, D. A., Balme, M. R., Conway, S. J., Wright, J., Pegg, D. L., Lennox, A. R., & Buoninfante, S. (2023). Geology of the Neruda quadrangle (H13), Mercury. *Journal of Maps*, *19*(1), 1–14. https://doi.org/10.1080/17445647.2023.2256353

Mancinelli, P., Minelli, F., Pauselli, C., & Federico, C. (2016). Geology of the Raditladi quadrangle, Mercury (H04). *Journal of Maps*, *12*(sup1), 190–202. https://doi.org/10.1080/17445647.2016.1191384

Marchi, S., Chapman, C. R., Fassett, C. I., Head, J. W., Bottke, W. F., & Strom, R. G. (2013). Global resurfacing of Mercury 4.0-4.1 billion years ago by heavy bombardment and volcanism. *Nature*, *499*(7456), 59–61. https://doi.org/10.1038/nature12280

Massironi, M., & Byrne, P. K. (2015). High-relief ridge. In H. Hargitai, & Á Kereszturi (Eds.), *Encyclopedia of planetary landforms* (pp. 932–934). Springer. https://doi.org/10.1007/978-1-4614-3134-3

Massironi, M., Byrne, P. K., & van der Bogert, C. H. (2015). Lobate scarp. In H. Hargitai, & Á Kereszturi (Eds.), *Encyclopedia of planetary landforms* (pp. 1255–1262). Springer. https://doi.org/10.1007/978-1-4614-3134-3

Massironi, M., Cremonese, G., Marchi, S., Martellato, E., Mottola, S., & Wagner, R. J. (2009). Mercury's geochronology revised by applying model production function to Mariner 10 data: Geological implications. *Geophysical Research Letter*, *36*(21), L21204. https://doi.org/10.1029/2009GL040353

McCauley, J. F., Guest, J. E., Schaber, G. G., Trask, N. J., & Greeley, R. (1981). Stratigraphy of the Caloris basin, Mercury. *Icarus*, *47*(2), 184–202. https://doi.org/10.1016/0019-1035(81)90166-4

McGill, G. E., & King, E. A. (1983). *Geologic Map of the Victoria (H–2) Quadrangle of Mercury*. USGS Miscellaneous Investigations Series, Map I–1409.

Melosh, H. J. (1996). *Impact cratering: A geologic process*. Oxford Monographs on Geology and Geophysics 11.

Murray, B. C. (1975). The Mariner 10 pictures of Mercury: An overview. *Journal of Geophysical Research*, *80*(17), 2342–2344. https://doi.org/10.1029/JB080i017p02342

Neukum, G., Oberst, J., Hoffmann, H., Wagner, R., & Ivanov, B. A. (2001). Geologic evolution and cratering history of Mercury. *Planetary and Space Science*, *49*(14-15), 1507–1521. https://doi.org/10.1016/S0032-0633(01)00089-7

Orgel, C., Fassett, C. I., Michael, G., Riedel, C., van der Bogert, C. H., & Hiesinger, H. (2020). Re-examination of the population, stratigraphy, and sequence of Mercurian basins: Implications for Mercury's early impact history and comparison with the Moon. *Journal of Geophysical Research: Planets*, *125*(8), 1–26. https://doi.org/10.1029/2019JE006212

Ostrach, L. R., Robinson, M. S., Whitten, J. L., Fassett, C. I., Strom, R. G., Head, J. W., & Solomon, S. C. (2015). Extent, age, and resurfacing history of the northern smooth plains on Mercury from MESSENGER observations. *Icarus*, *250*, 602–622. https://doi.org/10.1016/j.icarus.2014.11.010

Pegg, D. L., Rothery, D. A., Balme, M. R., & Conway, S. J. (2021b). Explosive vent sites on Mercury: Commonplace multiple eruptions and their implications. *Icarus*, *365*, 114510. https://doi.org/10.1016/j.icarus.2021.114510

Pegg, D. L., Rothery, D. A., Balme, M. R., Conway, S. J., Malliband, C. C., & Man, B. (2021a). Geology of the Debussy quadrangle (H14), Mercury. *Journal of Maps*, *17*(2), 718–729. https://doi.org/10.1080/17445647.2021.1996478

Robinson, M. S., Murchie, S. L., Blewett, D. T., Domingue, D. L., Hawkins, S. E., III, Head, J. W., Holsclaw, G. M., McClintock, W. E., McCoy, T. J., McNutt, R. L., Jr., Prockter, L. M., Solomon, S. C., & Watters, T. R. (2008). Reflectance and color variations on Mercury: Regolith processes and compositional heterogeneity. *Science*, *321*(5885), 66–69. https://doi.org/10.1126/science.1160080

Rothery, D. A. (2015). *Planet Mercury: From pale pink dot to dynamic world*. Springer. https://doi.org/10.1007/978-3-319-12117-8.

Rothery, D. A., Massironi, M., Alemanno, G., Barraud, O., Besse, S., Bott, N., Brunetto, R., Bunce, E., Byrne, P., Capaccioni, F., Capria, M. T., Carli, C., Charlier, B., Cornet, T., Cremonese, G., D'Amore, M., De Sanctis, M. C., Doressoundiram, A., Ferranti, L., … Zambon, F. (2020). Rationale for BepiColombo studies of Mercury's surface and composition. *Space Science Reviews*, *216*(4), 1–46. https://doi.org/10.1007/s11214-020-00694-7

Rothery, D. A., Thomas, R. J., & Kerber, L. (2014). Prolonged eruptive history of a compound volcano on Mercury: Volcanic and tectonic implications. *Earth and Planetary Science Letters*, *385*, 59–67. https://doi.org/10.1016/j.epsl.2013.10.023

Schaber, G. G., & McCauley, J. F. (1980). *Geologic Map of the Tolstoj (H–8) Quadrangle of Mercury*. USGS Miscellaneous Investigations Series, Map I–1199.

Skinner, J. A., Huff, A. E., Black, S. R., Buban, H. C., Fortezzo, C. M., Gaither, T. A., Hare, T. M., & Hunter, M. A. (2022). *Planetary geologic mapping Protocol 2022: U.S. Geological Survey Techniques and Methods 11-B13*.

Solomon, S. C., & Anderson, B. J. (2018). The MESSENGER mission: Science and implementation overview. In S. C. Solomon, L. R. Nittler, & B. J. Anderson (Eds.), *Mercury: The view after MESSENGER* (Vol. 21, pp. 1–29). Cambridge Univ. Press.

Solomon, S. C., McNutt, R. L., Gold, R. E., Acuña, M. H., Baker, D. N., Boynton, W. V., Chapman, C. R., Cheng, A. F., Gloeckler, G., Head, J. W., III, Krimigis, S. M., McClintock, W. E., Murchie, S. L., Peale, S. J., Phillips, R. J., Robinson, M. S., Slavin, J. A., Smith, D. E., Strom, R. G., … Zuber, M. T. (2001). The MESSENGER mission to Mercury: Scientific objectives and implementation. *Planetary and Space Science*, *49*(14-15), 1445–1465. https://doi.org/10.1016/S0032-0633(01)00085-X

Spudis, P. D., & Guest, J. E.. (1988). Stratigraphy and geologic history of Mercury. In F. Vilas, C. R. Chapman, & M. S. Matthews (Eds.), *Mercury* (pp. 118–164). University of Arizona Press. ISBN: 081651085.

Spudis, P. D., & Prosser, J. G. (1984). *Geologic Map of the Michelangelo Quadrangle of Mercury*. USGS Miscellaneous Investigations Series, Map I–1659.

Strom, R. G., Malin, M. C., & Leake, M. A. (1990). *Geologic Map of the Bach (H-15) Quadrangle of Mercury*. USGS Miscellaneous Investigations Series, Map I-2015.

Strom, R. G., Trask, N. J., & Guest, J. E. (1975). Tectonism and volcanism on Mercury. *Journal of Geophysical Research*, *80*(17), 2478–2507. https://doi.org/10.1029/JB080i017p02478

Tanaka, K. L., Skinner, J. A., Jr., & Hare, T. M. (2011). *Planetary geologic mappers handbook*. USGS Astrogeology Science Center. http://astrogeology.usgs.gov/search/details/Docs/Mappers/PGM_Handbook_2011/pdf

Thomas, R. J., Rothery, D. A., Conway, S. J., & Anand, M. (2014a). Long-lived explosive volcanism on Mercury. *Geophysical Research Letters*, *41*(17), 6084–6092. https://doi.org/10.1002/2014GL061224

Thomas, R. J., Rothery, D. A., Conway, S. J., & Anand, M. (2014b). Hollows on Mercury: Materials and mechanisms involved in their formation. *Icarus*, *229*, 221–235. https://doi.org/10.1016/j.icarus.2013.11.018

Tobler, W. (1987). Measuring spatial resolution. In *Land Resources Information Systems Conference* (pp. 12–16).

Trask, N. J., & Dzurisin, D. (1984). *Geologic Map of the Discovery (H-11) Quadrangle of Mercury*. USGS Miscellaneous Investigations Series, Map I-1658

Trask, N. J., & Guest, J. E. (1975). Preliminary geologic terrain map of Mercury. *Journal of Geophysical Research*, *80*(17), 2461–2477. https://doi.org/10.1029/JB080i017p02461

Wang, Y., Xiao, Z., Chang, Y., & Cui, J. (2020). Lost volatiles during the formation of hollows on Mercury. *Journal of Geophysical Research: Planets*, *125*(9), e2020JE006559. https://doi.org/10.1029/2020JE006559

Whitten, J. L., Head, J. W., Denevi, B. W., & Solomon, S. C. (2014). Intercrater plains on Mercury: Insights into unit definition, characterization, and origin from MESSENGER datasets. *Icarus*, *241*, 97–113. https://doi.org/10.1016/j.icarus.2014.06.013

Wright, J., Rothery, D. A., Balme, M. R., & Conway, S. J. (2019). Geology of the Hokusai quadrangle (H05), Mercury. *Journal of Maps*, *15*(2), 509–520. https://doi.org/10.1080/17445647.2019.1625821